

Experimental setup for the investigation of bubble mediated gas exchange

Wolfgang Mischler^{1,2}, Roland Rocholz² and Bernd Jähne^{1,2}

¹ *Heidelberg Collaboratory for Image Processing, University of Heidelberg,
Speyerer Straße 6, 69115 Heidelberg, Germany*

² *Institute for Environmental Physics, University of Heidelberg, Im
Neuenheimer Feld 229 6, 69120 Heidelberg, Germany
contact E-Mail: Wolfgang.Mischler@iup.uni-heidelberg.de*

Abstract. An experimental setup for the measurement of the contribution of air bubbles to gas exchange is presented. The bubble size distribution was measured as a function of the position in a 1.3m deep glass tank using an imaging method based on the *depth from focus* principle. Bubble radii from 100 to 1000 μm can be resolved with the recent image processing algorithm. The optical apparatus is automated to move horizontally and vertically along the tank walls in order to capture the whole bubble cloud. The bubble cloud is generated by a water jet which impinges on the water surface from above. The bubble distribution is similar to that produced by whitecaps, but stationary in a statistical sense. The flow rate of the air entrainment can be controlled. In a pilot experiment, the evasion of a set of trace gases was measured by means of UV absorption spectroscopy. The effect of the tracer solubility on the bubble-mediated gas exchange is demonstrated.

Key Words: bubble spectra, depth-from-focus, bubble-mediated gas exchange, imaging techniques

1. Introduction

In the ocean, bubble clouds are generated primarily by breaking waves and potentially contribute to the exchange of trace gases between ocean and atmosphere in a significant way (De Leeuw and Leifer (2002)). Since bubble mediated gas transfer is not well understood, the lab experiments aim at validating existing models and developing new models for the contribution of bubbles to gas transfer. Despite the progress in theoretical descriptions of bubble mediated gas transfer (Woolf et al. (2007), Keeling (1993), and Merlivat and Memery (1983)), there is still a lack of experimental studies validating these models. There have been various lab experiments with tipping buckets (Asher et al. (1995)) or in wind-wave tanks (Leifer and De Leeuw (2002)), which studied the gas transfer rate with varying whitecap coverage, solubility and diffusion constants or the size distribution of bubble clouds in breaking wind-waves. The residence time of a bubble depends on its radius, whereas the characteristic time for gas-exchange at the bubble surface depends (amongst others) on the solubility. Generally speaking, the residence time is larger for smaller bubbles and the exchange time is larger for smaller solubilities. Thus, in a bubble cloud, smaller bubbles reach equilibrium if their residence time is large compared to the exchange time. For small bubbles, the gas exchange is therefore directly related to the volume flux of these bubbles through the water surface. In the limiting case of infinitely high solubilities the whole bubble comes into equilibrium and the mean transfer velocity is given by (Woolf et al. (2007))

$$k_B^\infty = \frac{\dot{V}_B}{\alpha A_{ws}}, \quad (1)$$

where α is the dimensionless solubility, \dot{V}_B is the total volume flux of bubbles, and A_{ws} is the water surface area.

In contrast, in the limiting case of low solubilities, where bubbles may not come into equilibrium before they reach the surface, the gas exchange is effectively enhanced by the amount of additional surface area. For very low solubilities, the surface area of the whole bubble cloud acts as additional exchange surface. If the bubble size distribution, $\Psi_A(r)$ ¹, is known then the mean transfer velocity of the bubble cloud can be expressed as

$$k_B^0 = \int 4\pi r^2 \Psi_A(r) k_B(r) dr = \int \gamma(r) k_B(r) dr. \quad (2)$$

¹The bubble size distribution gives the number of bubbles per radius increase, dr , in the range $[r, r + dr]$ per unit area of the water surface.

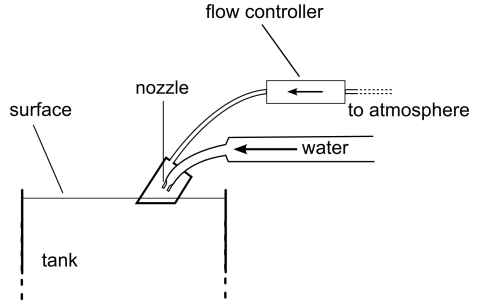


Figure 1. Experimental setup

Here, $k_B(r)$ denotes the transfer velocity at a single bubble and $\gamma(r)$ denotes the bubble surface to water surface ratio per radius interval, dr .

Our experiment is designed to investigate the relationship between the gas transfer velocity and the solubility/diffusion constant with a known size-distribution at defined conditions. The long-term intention is to measure or control all variables of the prevailing parameterizations, so that the models can be compared and improved eventually. As a first step, an optical method for the measurement of the bubble size distribution $\Psi_A(r)$ was implemented (see section 3.). The total volume flux of the bubbles, \dot{V}_B , is controlled by a flow meter. The water sided tracer concentrations are measured with UV-Spectroscopy. A proof-of-concept experiment was carried out that shows the effect of solubility on the bubble-mediated gas exchange (see sections 4. and 5.).

2. Setup

For the experiment a glass tank ($130 \text{ cm} \times 70 \text{ cm} \times 15 \text{ cm}$, $H \times W \times D$) was built, see fig. 1. It is designed to be chemically resistant to a large set of substances in order to cover a wide range of solubilities and diffusion constants. The bubbles are generated by a water jet which is supplied by water taken from the bottom of the tank. The jet entrains air out of a closed volume, which is connected to the atmosphere through a flow controller (see fig. 1). The jet

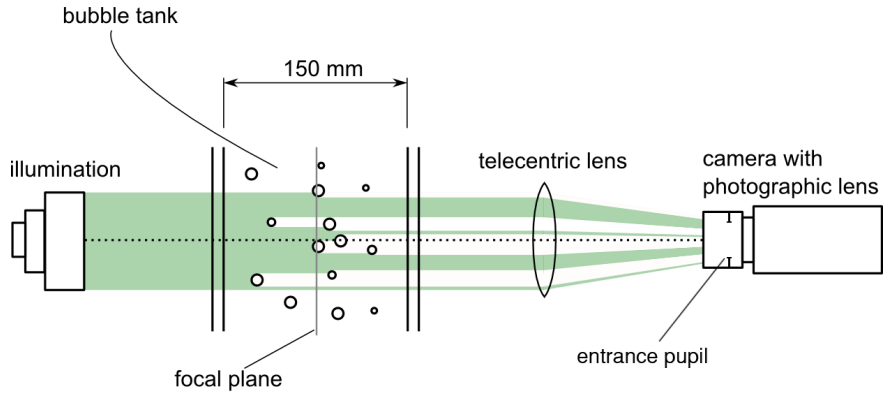


Figure 2. Illustration of the telecentric setup. A camera with a 35 mm photographic lens at a relative aperture of 8 is used. The entrance pupil of the camera is in focal distance to a second lens with a focal length of 160 mm and a diameter of 50.8 mm to yield telecentric imaging. For the illumination a photographic lens with an LED in its focal plane is used.

is adjusted in a way that the rising bubbles reach the surface outside of this closed air volume. The jet generated bubble clouds in this setup show a size distribution, which is similar to those generated by breaking wind waves (Deane and Stokes (2002)). Water sided tracer concentrations are measured with UV absorption spectroscopy (Degreif (2006)).

3. Optical measurement of bubble size distribution

The optical setup for measuring the bubble size distribution is shown in fig. 2. It is mounted on translation stages to allow for measurements at all positions of the tank. The setup consists of a telecentric optic and a telecentric illumination, which are used in a bright field configuration based on the setup that was presented by Jähne and Geißler (1995). The telecentricity gives the advantage of a constant magnification factor over the whole measurement volume. Moreover, it leads to a definite dependency between the focus/defocus of the bubble and its distance, z , to the focal plane. When the bubbles move into focus they appear sharp, when they move out of focus they gradually appear blurred. The camera looks into a telecentric illumination, which is used to illuminate an angle of $\pm 1.8^\circ$. Because of the small angle, the images of the bubbles appear as dark

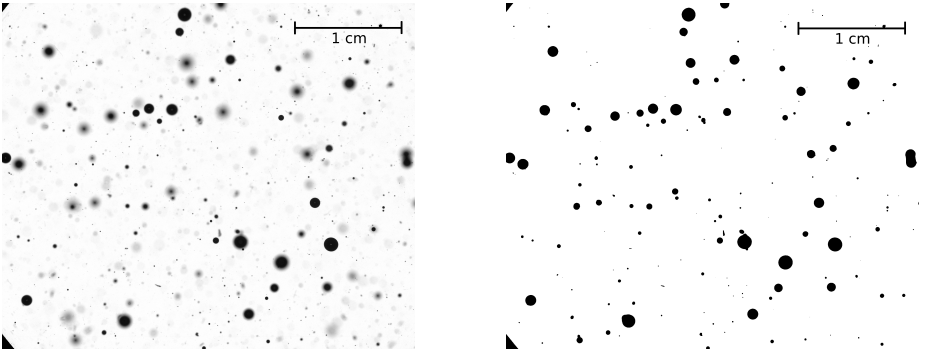


Figure 3. left: Normalized image; right: segmented at 50%; 1 px corresponds to $16 \mu\text{m}$ ($2050 \text{ px} \times 2448 \text{ px}$; $3.3 \text{ cm} \times 3.9 \text{ cm}$)

disks, since almost all of the light is scattered out of the optical path (see fig. 3 and Jähne and Geißler (1995)).

Images are projections from 3D-space into 2D-space. In order to determine the measurement volume, which is needed for calculating bubble densities, it is necessary to know the z-range, in which the bubbles can be detected. Here, defocus is used as a measure for the distance to the focal plane, so that the z-range of the measurement volume is determined by a certain degree of defocus. Ordinary optics have a magnification factor that depends on the distance. This effect occurs simultaneously to the defocus, which complicates the evaluation of size and distance. Therefore, a telecentric optic is used to avoid these problems (see Mischler (2010)). A sample image is shown in fig. 3 left. To simplify further processing and to reduce noise, the images $g(x, y)$ are normalized with a dark image g_D (no illumination) and a zero image g_Z (illumination, but no bubbles)

$$n(x, y) = \frac{g(x, y) - g_D(x, y)}{g_Z(x, y) - g_D(x, y)}, \quad (3)$$

where $n(x, y)$ is the resulting normalized image (a value of one corresponds to background and a value of zero corresponds to a bubble). A bubble in the focal plane appears as a sharp disk in the image. With increasing distance to the focal plane the disk edge becomes blurred (defocus) and the gray value gradually gets higher. Because of the loss in contrast, bubbles that are too far away from the focal plane cannot be measured. The critical distance depends on the bubble size. Hence, the effective measurement volume depends on the bubble radius -

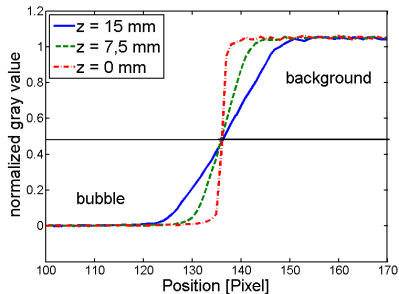


Figure 4. Gradient on the edge as a function of distance from the focal plane

large bubbles exhibit a greater measurement volume than small bubbles.

As can be seen in fig. 4, the gradient of the disk edge depends on the distance (defocus effect), whereby the position of the edge remains constant (constant magnification factor). The gradient of the gray value n at the edge position is given by

$$\frac{\partial}{\partial x} n|_{edge} = \frac{1}{(z \cdot \tan \beta)^2}, \quad (4)$$

where z denotes the distance from the focal plane and β the opening angle of the recording optics (see fig. 4 and Mischler (2010)). Equation (4) is true as long as the intensity reaches its minimum in the center of the bubble. Since this constraint depends on the size of the bubbles², the maximal z -range depends on the bubble size. For example the maximal z -range is 3.3 mm for bubbles of $100 \mu\text{m}$ size and 14 mm for bubbles of $300 \mu\text{m}$ size. The telecentric setup simplifies the evaluation of the parameters size and 3D position³. The magnification factor and the relationship between depth and defocus are determined through gauge-series with aperture targets.

3.1 Algorithm

For each measurement position, several hundred images with five mega pixels ($2050 \text{ px} \times 2448 \text{ px}$) are taken and the data is evaluated automatically. The algorithm is able to separate overlapping bubbles and determine their 3D position and radius. The position at half maximum corresponds to the true position of the edge (Jähne and Geißler (1995)). Due to the normalization

²because the z -dependent point-spread-function has to be smaller than the object itself

³there is an ambiguity in the z -position, because it is not possible to decide whether the object is in front of or behind the focal plane

this equals a value of 0.5 in the image, which is used as a global threshold for segmentation and labeling. The contour of each object is calculated and used for the separation of overlapping bubbles, based on the idea of Honkanen et al. (2005). Overlapping bubbles exhibit a high negative curvature at locations where two or more bubble projections overlap. The contour is cut at these points and a circle is fitted at each resulting segment. These circles are clustered because more than one segment can belong to the same bubble. A measure of the clustering is given by the ratio, ϵ , of the distance of the center points, Δx , to the difference of the radii, Δr ,

$$\epsilon = \frac{\Delta x}{\Delta r}. \quad (5)$$

Here, a threshold of $\epsilon = 0.6$, a minimal segment length of $\frac{1}{10}r$ and a maximal number of segments per object of 9 were experimentally chosen. The minimal segment length and maximal segments per object are used to reject non-bubble objects and objects that consist of several overlapping bubbles which may not be detected reliably.

For each detected bubble, it is checked if the minimum gray value is reached at the center point to be sure that the bubble is inside the defined measurement volume.

Because of possible occlusion, the area in the image that is occupied by the projections of bigger bubbles reduces the image area that is available for the detection of all the smaller bubbles. In order to get correct bubble densities, the effective area needs to be computed for each bubble radius, based on the given image data. For this, the area that is covered by all bigger bubbles is subtracted from the image area that is used to compute the effective measurement volume for a given radius (Mischler (2010)).

3.2 Validation of the algorithm

Synthetic images with a specified size-distribution were generated to check the performance of the algorithm. The images were produced by a physical model which takes geometric and diffraction effects, but not bubble geometry⁴, into account (see Mischler (2010)). About 500 images with a size of 1000 px × 1000 px with 500 bubbles each were processed. The bubbles in the synthetic images have a distribution proportional to r^{-3} , which is compared to the results of the algorithm in fig. 5. It can be seen that in a size range from 10 px to 100 px (which corresponds a range of 160 μm to 1600 μm) the deter-

⁴which is reasonable, since in focus bubbles appear as dark disks in this setup

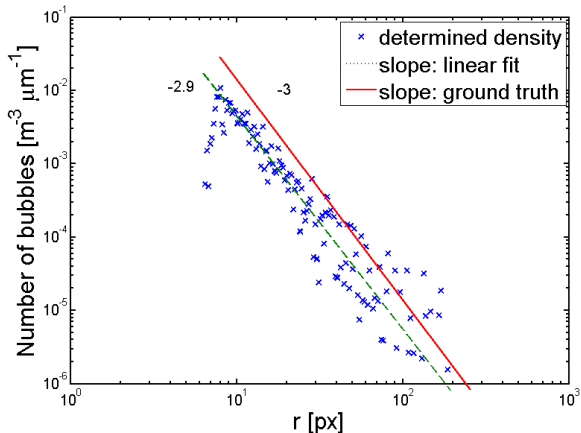


Figure 5. Size distribution determined by used algorithm in comparison with ground truth

mined values can be used. The statistical error of the fitted slope is 0.2 or 7 percent, which is caused by errors in determining the bubble size.

4. Experiments

A proof-of-concept gas-exchange experiment was conducted with three different tracers with almost identical diffusivities D , but very different solubilities, α , ranging from 0.1 to 13.7, see table 1. This enables the investigation of the dependency of bubble mediated gas transfer on solubility. The concentrations of the tracers were measured simultaneously over a period of five hours. The water jet was adjusted in a way that the generated bubble cloud covered a maximal area of the frontal plane at an inward volume flux of $\dot{V}_B = 2.2 \frac{1}{\text{min}}$ of entrained air. The bubble distributions were measured at eleven positions on a vertical profile 50 cm away from the point the jet penetrates the water surface. Images were taken over the whole period of the experiment, whereby 48 images were taken at each position before the next position was approached.

5. Results

In fig. 6 the results of the bubble density measurements are shown. Throughout the experiment the observed bubble distribution remained stationary. The

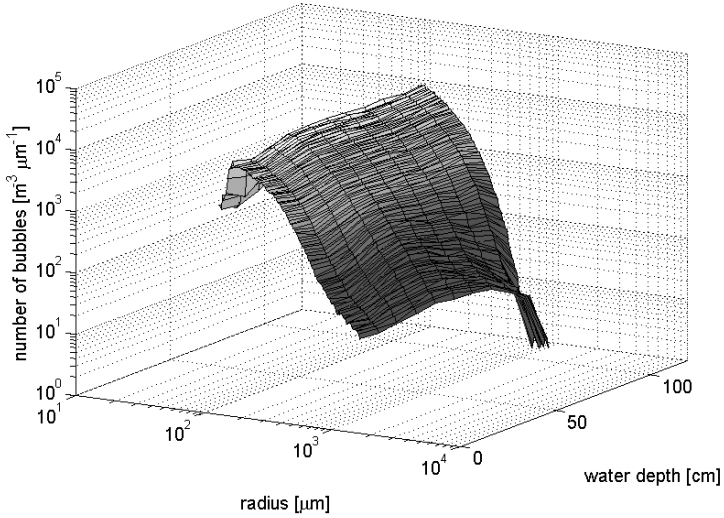


Figure 6. Measured size distribution profile

averaged distribution is shown in the plot. Large bubbles are less numerous in regions far away from the surface, which is expected since these bubbles have a faster rise velocity and therefore have shorter residence times than small bubbles and hence rarely reach deep regions. The small bubbles are almost uniformly distributed because their buoyancy is not strong enough to overcome the strong jet-generated currents in the tank. The slight increase of the bubble density at a depth of 50 cm arises from the crossing jet, which carries the majority of all bubbles with it. A fit of the distribution for a radius smaller than $400 \mu\text{m}$ gives a dependency of the number density proportional to r^{-2} and for bubble radii greater than $400 \mu\text{m}$ a dependency proportional to $r^{-3.5}$. This is similar to the power law behavior of bubble plumes of breaking waves as found by Deane and Stokes (2002), i.e. $r^{-3/2}$ for radii smaller than 1 mm, $r^{-10/3}$ for radii greater than 1 mm. Here, the transition occurs at a lower critical radius of $400 \mu\text{m}$, which might be attributed to the different mechanism of bubble creation and the usage of pure water instead of salt water.

In table 1 the results for the gas exchange times τ , i.e. the time in which the concentration of the tracer in the tank falls to a fraction $\frac{1}{e}$, are shown. The experimental results τ_{exp} represent the values evaluated from the UV absorp-

Tracer	$\tau_{exp}[\text{s}]$	$\tau_{min}[\text{s}]$	α_{lit}	$D[\frac{\text{cm}^2}{\text{s}}]$
Hexafluorbenzene	9500 ± 30	300 ± 150	0.10 ± 0.05	0.85
1,4-Difluorbenzene	13900 ± 30	10000 ± 5000	3.2 ± 1.6	0.94
Phenylacetylene	21300 ± 70	43000 ± 21500	13.7 ± 6.9	0.84

Table 1. Comparison of measured and expected minimum gas exchange times. The exchange time is the time in which the concentration in the tank falls to a fraction of $\frac{1}{e}$. The considerable uncertainty of the solubility of the used tracers and their temperature dependency lead to large errors in the calculated minimal gas exchange time τ_{min} .

tion spectroscopy measurements and the expected minimum values τ_{min} are calculated through equation (1), which yields

$$\tau_{min} = \frac{h_{Tank}}{k_B^\infty} = \alpha \frac{V_{tank}}{\dot{V}_B}, \quad (6)$$

with $V_{tank} = 115$ liter being the water volume, and $h_{tank} = 110$ cm the height of the water column. Since this approximation considers all bubbles in equilibrium it is expected that it systematically delivers lower τ_{min} values than the measured τ_{exp} . The measured exchange time for phenylacetylene is slightly outside the error range of the expected minimal value, which might be explained by the poorly known solubility of this tracer. However, the qualitative effect of solubility can be seen already by comparison of the experimental values τ_{exp} . For the estimation of the effective bubble mediated transfer velocity, k_B , the residence time of the bubbles as a function of radius must be known. The residence time can be inferred from the size distribution and radius resolving measurements of the bubble-flux through the surface. A method for the latter is currently under development.

The bubble surface calculated from the measured size distribution gives a ratio of total bubble surface to water surface area in the plume (at the position of the profile) of about $\gamma = 3$. Taking into account that only a portion of the radius spectrum could be measured, this highlights that the gas exchange times measured in our tank are dominated by the bubble cloud.

6. Conclusions and outlook

The bubble size distribution and tracer concentrations measurements in the new Heidelberg bubble tank showed qualitative agreement with the expected dependence of the gas exchange time on the solubility. The measurement of the size distribution was improved versus Jähne and Geißler (1995) using new image processing algorithms and a high resolution camera. To avoid the error of extrapolation of the bubble distribution, the whole bubble cloud can be scanned in following experiments. In order to calculate the transfer velocities the bubble flux through the surface is needed. A method for this task is under development.

References

- Asher, W. E., L. M. Karle, B. J. Higgins, P. J. Farley, I. S. Leifer, and E. C. Monahan (1995), The effect of bubble plume size on the parameterization of air-seawater gas transfer velocities, *Proceedings of the 3rd International Symposium on Air-Water Gas Transfer*. (Eds. B. Jähne and E. Monahan), AEON, Hanau, 351–362.
- Deane, G. B. and M. D. Stokes (2002), Scale dependence of bubble creation mechanisms in breaking waves, *Nature*, *418*(6900), 839–844.
- Degreif, K. (2006), *Untersuchungen zum Gasaustausch - Entwicklung und Applikation eines zeitlich aufgelösten Massenbilanzverfahrens*, Dissertation, Institut für Umweltphysik, Fakultät für Physik und Astronomie, Univ. Heidelberg.
- Honkanen, M., P. Saarenrinne, T. Stoor, and J. Niinimäki (2005), Recognition of highly overlapping ellipse-like bubble images, *Meas. Sci. Technol.*, *16*(9), 1760–1770.
- Jähne, B. and P. Geißler (1995), An imaging optical technique for bubble measurements, *Proc. Sea Surface Sound '94*. (Eds. M. J. Buckingham and J. R. Potter), Singapore, 290–296.
- Jähne, B., T. Wais, and M. Barabas (1984), A new optical bubble measuring device; a simple model for bubble contribution to gas exchange, *Gas transfer at water surfaces*. (Eds. W. Brutsaert and G. H. Jirka), Reidel, Hingham, MA, 237–246.
- Keeling, R. F. (1993), On the role of large bubbles in air-sea gas exchange and supersaturation in the ocean, *J. Mar. Res.*, *51*, 237–271.
- De Leeuw, G. and I. Leifer (2002), Bubbles outside the plume during the luminy wind-wave experiment, *Gas Transfer at Water Surfaces*. (Eds. M. A. Donelan, W. M. Drennan, E. S. Saltzman, R. Wanninkhof), *Geophysical Monograph*, *127*, 295–301.

- Leifer, I. and G. De Leeuw (2002), Bubble measurements in breaking-wave generated bubble plumes during the luminy wind-wave experiment, *Gas Transfer at Water Surfaces*. (Eds. M. A. Donelan, W. M. Drennan, E. S. Saltzman, and R. Wanninkhof), *Geophysical Monograph*, 127, 303–309.
- Merlivat, L. and L. Memery (1983), Gas exchange across an air-water interface: experimental results and modeling of bubble contribution to transfer, *J. Geophys. Res.*, 88, 707–724.
- Mischler, W. (2010), *Entwicklung eines Experiments zur Messung von Blasendichten und blaseninduziertem Gasaustausch*, Diplomarbeit, Institut für Umweltphysik, Fakultät für Physik und Astronomie, Univ. Heidelberg. http://hci.iwr.uni-heidelberg.de/publications/dip/2010/mischler_2010.pdf
- Sander, R. (1999), Compilation of henry’s law constants for inorganic and organic species of potential importance in environmental chemistry (version 3).
- Wolf, D. (1997), Bubbles and their role in gas exchange, *The sea surface and global change*. (Eds. P. S. Liss and R. A. Duce), Cambridge Univ Press, 173–205.
- Wolf, D., I. Leifer, P. Nightingale, T. Rhee, P. Bowyer, G. Caulliez, G. de Leeuw, S. Larsen, M. Liddicoat, J. Baker, and M. Andreae (2007), Modelling of bubble-mediated gas transfer: Fundamental principles and a laboratory test, *J. Mar. Syst.*, 66, 71–91.